Shubnikov–de Haas oscillations in topological crystalline insulator SnTe(111) epitaxial films

A. K. Okazaki,[1,*] S. Wiedmann,[2] S. Pezzini,[2,†] M. L. Peres,[3] P. H. O. Rappl,[1] and E. Abramof[1]

[1]*Laboratório Associado de Sensores e Materiais, Instituto Nacional de Pesquisas Espaciais, São José dos Campos, CEP 12201-970 São Paulo, Brazil*

[2]*High Field Magnet Laboratory EMFL and Institute for Molecules and Materials, Radboud University, 6525 ED Nijmegen, The Netherlands*

[3]*Instituto de Física e Química, Universidade Federal de Itajubá, Itajubá, CEP 37500-903 Minas Gerais, Brazil*

(Received 13 September 2018; revised manuscript received 26 October 2018; published 26 November 2018)

We report on high-field (up to 30 T) magnetotransport experiments in topological crystalline insulator (111) SnTe epitaxial films. The longitudinal magnetoresistance R_{xx} exhibits pronounced Shubnikov–de Haas (SdH) oscillation at 4.2 K that persists up to 80 K. The second derivative ($-d^2R_{xx}/dB^2$) versus $1/B$ curve shows a clear beating pattern and the fast Fourier-transform analysis reveals that the SdH oscillations are composed of two close frequencies. As SnTe has elongated bulk Fermi ellipsoids, the $1/\cos\theta$ dependence obtained in the angular evolution of both SdH frequencies is not sufficient to assure conduction via surface states. The Lifshitz-Kosevich fitting of the R_{xx} oscillatory component confirms the two frequencies and enables us to extract the Berry phase of the charge carriers. The most likely scenario obtained from our analysis is that the beating pattern of these quantum oscillations originates from the Rashba splitting of the bulk longitudinal ellipsoid in SnTe.

DOI: 10.1103/PhysRevB.98.195136

I. INTRODUCTION

The topological classification of band structures was extended to include certain crystal point-group symmetries. This extension led to a new class of materials called topological crystalline insulators (TCIs), which present gapless metallic surface states in crystalline planes of high symmetry [1]. These topological surface states (TSSs) are protected by crystal symmetry and rises due to a nontrivial band-structure system. Tin telluride (SnTe) was predicted to be the first TCI material class [2] and, due to its nontrivial topology, the TSS appears with an even number of Dirac cones on high-symmetry crystal surfaces such as (001), (110), and (111).

The pseudobinary alloy $Pb_{1-x}Sn_xTe$ crystallizes in the rock-salt structure. Due to the inversion symmetry of this crystal structure and to the high anisotropy of the multivalley band structure, the surfaces of constant energy on these materials are given by elongated ellipsoids with a longitudinal valley parallel to the [111] direction and three other equivalent oblique valleys. Each ellipsoid is located at the L points in the Brillouin zone, which are the centers of the hexagonal faces [3,4] [see Figs. S1(a) and S1(b) in Supplemental Material [5]]. For this semiconductor compound, the band extrema occur at the L points with a direct and narrow energy gap. For pure PbTe the material is referred to as a trivial semiconductor where the L^{6-} and L^{6+} levels correspond to the conduction-band (CB) minimum and valence-band (VB) maximum, respectively. If Sn content is continuously increased, the energy gap of $Pb_{1-x}Sn_xTe$ decreases and vanishes for a critical Sn content x_c. A further increase up to the pure SnTe leads to an inverted band-structure regime with the L^{6+} state corresponding to the CB minimum and the L^{6-} corresponding to the VB maximum [6,7] [see Fig. S1(c) in Supplemental Material [5]]. The critical composition where the band gap vanishes varies from $x_c = 0.35$ at 4 K to $x = 0.63$ at 300 K. Due to the native Sn vacancies, bulk crystals and epilayers of SnTe always grow highly p doped ($\sim 10^{20}\,\mathrm{cm}^{-3}$) [8].

The first experimental evidence of a TCI was observed in a SnTe bulk crystal by angle-resolved photoemission spectroscopy (ARPES) [9], in which a metallic surface band in the format of a Dirac cone was observed in the ARPES spectrum of the (001) plane in the border of the $\bar{X}$ point along the $\bar{\Gamma}$-$\bar{X}$ linecut. Just after, ARPES measurements at 10 K in the (001) plane of a $Pb_{0.6}Sn_{0.4}Te$ bulk crystal, with a Sn content in the band inversion region for this temperature, proved the existence of an even number of spin-polarized Dirac cones, revealing a topological order by crystal symmetry. The absence of Dirac cones in the (001) surface of a $Pb_{0.8}Sn_{0.2}Te$ crystal, where the bands are not inverted, demonstrated experimentally the transition from a trivial insulator to a TCI in the PbSnTe system [10]. ARPES spectra measured in the (111) surface of SnTe [11] and PbSnTe [12,13] also revealed the Dirac cones in the $\bar{\Gamma}$ and $\bar{M}$ points in this plane [see Fig. S1(d) in Supplemental Material [5]].

Although the surface states are directly and clearly observable in ARPES spectra, probing the TSS by electrical transport experiments in three-dimensional (3D) topological insulators (TIs) is a challenge. The electronic transport through the TSS is always hampered by the bulk conduction in all 3D TI materials such as Bi_2Te_3 [14], Bi_2Te_2Se [15,16], and Bi_2Se_3 [17–20]. Even if the material is tailored to tune the Fermi level inside the band gap, the residual bulk defects still contribute to the parallel conduction. Usually, the surface contribution to the conduction in TI samples is indirectly

*anderson.okazaki@inpe.br

†Present address: Center for Nanotechnology Innovation @NEST, Istituto Italiano di Tecnologia, Piazza Di San Silvestro 12, 56127 Pisa, Italy.

obtained by the angular dependence of the Shubnikov–de Haas (SdH) oscillations in magnetotransport measurements.

In the case of SnTe, transport experiments are restricted to few works. There is a suggestion based on SdH experiments up to 14 T that Dirac fermions reside on the (111) surface of 30-nm-thick SnTe films grown on Bi_2Te_3 buffer layers, due to a downward band bending on the free SnTe surface [21]. In other investigations, information about Dirac surface states is inferred from modeling of low magnetic field weak antilocalization data measured on (001) and (111) SnTe thin films [22,23]. Magnetotransport (up to 13 T) and magnetization (up to 9 T) measurements on 0.4-mm-thick SnTe bulk crystal at tilted magnetic fields revealed SdH and de Haas–van Alphen oscillations, which were interpreted as experimental evidence of surface states on neighboring sample sides [24]. In that work the authors claim that the Femi energy is pinned to the SnTe bulk reservoir, which provides carriers for the TSS.

In this paper, we present a study based on high magnetic field (up to 30 T) magnetotransport experiments performed on (111) SnTe epitaxial films. Unlike the papers mentioned above, the longitudinal magnetoresistance measured in our SnTe films exhibited very clear and well-developed SdH oscillations at 4.2 K that persist up to 80 K. The fast Fourier-transform (FFT) analysis of the second derivative of these oscillations with respect to the magnetic field revealed that two frequencies close to each other contribute to the SdH effect. The cyclotron masses associated with these two frequencies are determined by fitting the temperature dependence of the FFT amplitude with the thermal term of the Lifshitz-Kosevich equation.

To find out whether the SdH oscillations originate from bulk or surface states (or from both), a set of analyses was performed. The contribution of the oblique bulk ellipsoidal Fermi surfaces to the oscillations is discarded by geometric arguments. The angle dependence of the SdH oscillations is determined by measuring the longitudinal magnetoresistance as a function of the tilt angle θ. A $1/\cos\theta$ dependence was found for the angular evolution of both SdH frequencies. In the case of SnTe, in contrast to other TI materials, this argument is not sufficient to guarantee surface conduction, since the elongated bulk Fermi ellipsoids also present this angular behavior.

The oscillatory component of the longitudinal magnetoresistance was isolated using the background subtraction method and fitted to the complete Lifshitz-Kosevich expression. The best fit was achieved considering the same two frequencies obtained from the FFT analysis and a different Berry phase was found for each frequency.

The most likely scenario obtained from the analysis of all these results is that the SdH oscillations observed in (111) SnTe epitaxial films consist of two oscillatory components arising from the splitting of the bulk longitudinal ellipsoid due to Rashba spin-orbit coupling.

II. EXPERIMENTS

Single-crystalline SnTe films with a thickness of 2 μm were grown on a (111) BaF_2 substrate by molecular-beam epitaxy in a Riber 32P system with a main chamber base pressure around 10^{-10} Torr. For the growth, we used a stoichiometric SnTe solid source and an additional Te cell to compensate the preferential Te evaporation. The growth rate was 8.6 nm/min.

Due to the lattice mismatch of 2% between SnTe and BaF_2, the growth starts with islands' nucleation and, after their coalescence around 60 nm, it turns to the step-flow mode and remains in this growth condition till the end. Atomic force microscopy (AFM) imagery of (111) SnTe films surface exhibits spiral-like triangular domains with terrace steps of $\sim$0.4 nm corresponding to one monolayer of SnTe, characteristic of a plain and smooth surface. The full width at half maximum of the (222) SnTe Bragg peak equals 197 arcsec, indicating the high crystalline quality of the films. The lattice constant of 0.6327 nm for SnTe films, measured at room temperature with respect to the BaF_2 substrate, demonstrates that 2-μm-thick films are completely relaxed [see Fig. S2 in Supplemental Material [5] for the reflection high-energy electron-diffraction (RHEED), AFM, and x-ray-diffraction analyses].

For the electrical characterization, sample pieces of approximately 9 mm^2 were prepared in van der Pauw geometry by soldering Au wires to SnTe films with In pellets. Before high magnetic field experiments, resistivity and low-field (0.7 T) Hall effect were measured from 12 to 300 K. SnTe films are found to be p type with a carrier concentration of $1.9 \times 10^{20}\,cm^{-3}$ independent of temperature. The resistivity is $2.2 \times 10^{-5}\,\Omega\,cm$ at 12 K and increases linearly to $1.7 \times 10^{-4}\,\Omega\,cm$ at 300 K. The Hall mobility saturates at a value of $1500\,cm^2/V\,s$ at low temperatures (see Fig. S3 in Supplemental Material [5] for the electrical characterization at low magnetic field).

The magnetotransport measurements were carried out in a ^{4}He flow cryostat with a rotation system placed in a 33-T resistive (Bitter-type) magnet, using standard four-probe ac lock-in technique with constant excitation current of 2.0 μA.

III. RESULTS AND DISCUSSION

The longitudinal resistance R_{xx} and Hall resistance R_{xy} measured at 4.2 K as a function of the magnetic field B applied perpendicular to the (111) sample surface are shown in Fig. 1(a).

The Hall resistance R_{xy} (red solid line) shows a linear behavior with superimposed low-amplitude oscillations. A linear fit to R_{xy} in the low-field regime ($B < 3$ T), shown by the dashed blue line, confirms the same carrier concentration ($p_{Hall} = 1.9 \times 10^{20}\,cm^{-3}$) and Hall mobility ($\mu = 1500\,cm^2/V\,s$) reported in Sec. II.

In contrast to previous works [21–24], the longitudinal resistance R_{xx} measured in SnTe films at 4.2 K exhibits clear and well-developed SdH oscillations. One can clearly distinguish a first less-intense set of SdH oscillations between 8 and 12 T and a second set with high amplitude from 12 to 30 T. To analyze these oscillations, we considered the second derivative of the longitudinal resistance with respect to the magnetic field ($-d^2R_{xx}/dB^2$), which is plotted in Fig. 1(b) as a function of the inverse field $1/B$. A clear beating pattern is visible in the graph, indicating the presence of (at least) two oscillatory components with close frequencies.

In order to discern the contributions involved in the SdH oscillations, we performed a FFT of the data plotted in the graph of Fig. 1(b), considering the field interval from 8 to 30 T.

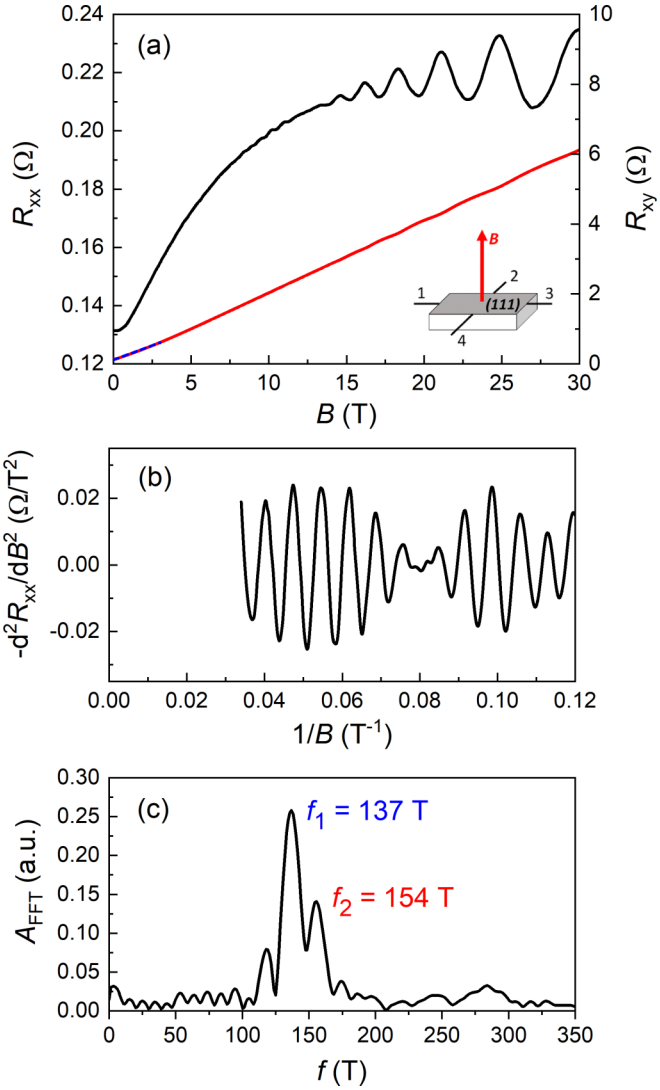

FIG. 1. (a) Longitudinal resistance R_{xx} (black line) and Hall resistance R_{xy} (red line) measured at 4.2 K as a function of magnetic field B applied perpendicular to the (111) SnTe/BaF_2 sample surface. The blue dashed line is a linear fit to R_{xy} for $B < 3$ T. (b) Second derivative of R_{xx} with respect to B as a function of $1/B$. (c) FFT amplitude as a function of frequency f, evidencing that two main close frequencies f_1 and f_2 compose the SdH oscillations.

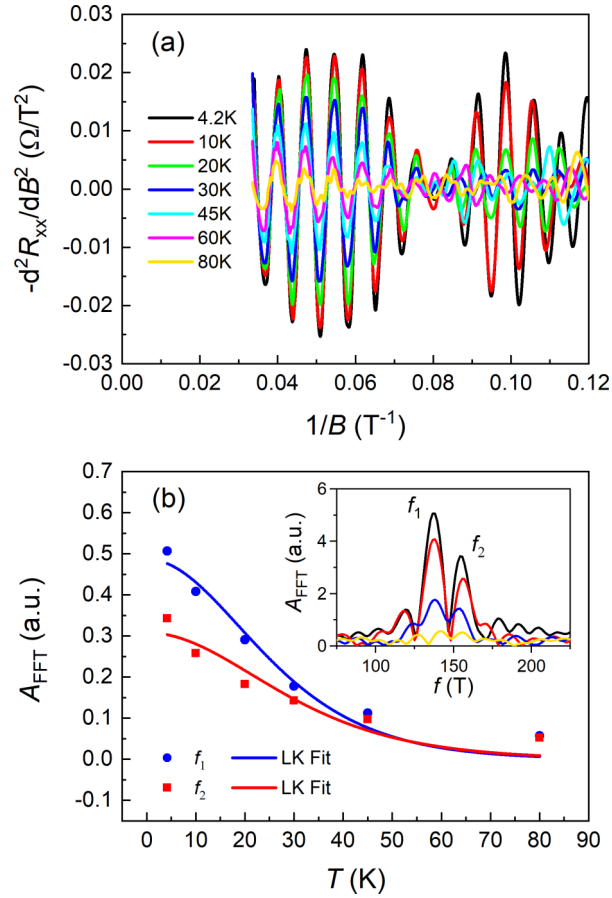

FIG. 2. (a) Temperature dependence of the SdH oscillations in the longitudinal resistance R_{xx} measured from 4.2 to 80 K. (b) FFT peak amplitude as a function of temperature for the frequencies f_1 and f_2. The solid curves are the best fits to the data using the thermodynamic term of the Lifshitz-Kosevich formula. Inset: FFT of the SdH oscillations presented in panel (a) with the same temperature color code.

The result is shown in Fig. 1(c), where two main frequencies $f_1 = 137$ T and $f_2 = 154$ T are identified. The third peak visible at 118 T is discarded since its intensity does not present a regular damping behavior as a function of temperature [inset of Fig. 2(b)]. Therefore, it can be treated as an artifact from the FFT analysis.

The cyclotron mass associated with the SdH oscillation frequency can be extracted from the temperature dependence of the oscillations. For this purpose, the longitudinal resistance $R_{xx}(B)$ was measured for increasing temperatures ranging from 4.2 to 80 K. The corresponding $-d^2R_{xx}/dB^2$ is plotted in Fig. 2(a) as a function of $1/B$.

The thermal damping of the FFT amplitude frequencies A_{FFT}, shown in the inset of Fig. 2(b), is described by the thermodynamic part of the Lifshitz-Kosevich (LK) equation:

$$A_{FFT} = A_0\left(\frac{2\pi^2 k_B}{e\hbar}\frac{m^*T}{\bar{B}}\right)/\sinh\left(\frac{2\pi^2 k_B}{e\hbar}\frac{m^*T}{\bar{B}}\right), \quad (1)$$

where A_0 is an adjustment constant, k_B is the Boltzmann constant, e is the elementary charge, $\hbar$ is the reduced Planck constant, T is the temperature, $\bar{B}$ is the inverse of the mean value of the $1/B$ interval used in the FFT analysis, and m^* is the cyclotron mass. The right-hand side of Eq. (1) corresponds to the second term of the complete LK expression given by Eq. (3). The FFT amplitude of the two main oscillatory components is shown as a function of temperature in Fig. 2(b), together with the best fits using Eq. (1). From the fitted curves, it was possible to extract the cyclotron mass for each frequency: $m_1^* = (0.077 \pm 0.005)m_e$ and $m_2^* = (0.067 \pm 0.008)m_e$, where m_e is the free-electron mass. These values, compatibles within error bars, are very close to the ones found in the literature for SnTe [21,24].

The SdH quantum oscillation frequency f is directly proportional to the extremal cross-sectional area S_F, of the Fermi surface perpendicular to the applied magnetic field, according

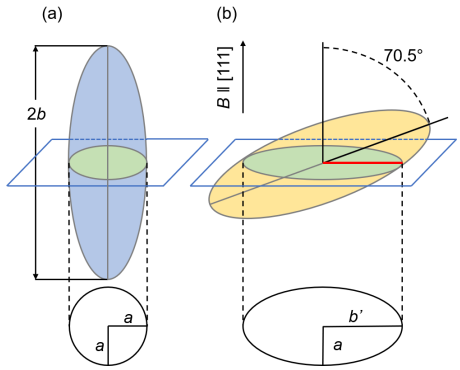

FIG. 3. Representation of the (a) longitudinal and (b) oblique ellipsoidal Fermi surfaces of SnTe. For a magnetic field B applied parallel to the [111] direction, the extremal cross-sectional area of the tilted ellipsoid (oblique valley) is 2.1 times larger than the one of the parallel ellipsoid (longitudinal valley), due to the 70.5° inclination.

to the Onsager relation:

$$f = \left(\frac{\hbar}{2\pi e}\right) S_F. \tag{2}$$

The Fermi wave vector k_F can be obtained considering a circular cross-sectional area $S_F = \pi k_F^2$. Thus, the Fermi wave vectors calculated for each frequency are $k_{F1} = 0.0645$ Å^{-1} and $k_{F2} = 0.0684$ Å^{-1}. Also, the Fermi velocity $v_F = \hbar k_F / m^*$ of the carriers can be calculated and a value around $v_F = 1 \times 10^6$ m/s is obtained for both SdH frequencies, similar to other values obtained for SnTe by ARPES [9] and SdH oscillations [21,24].

Next, after establishing the presence of two components in the SdH oscillations of TCI SnTe thin films, it is now fundamental to understand whether these oscillations arise from surface or bulk channels. Figure 3 shows a representation of the longitudinal and oblique bulk ellipsoidal Fermi surfaces of SnTe. The anisotropy factor of these Fermi pockets is defined as $K = (b/a)^2$, where b is the semimajor axis and a is the semiminor axis of the ellipsoid. This factor is equivalent to the anisotropy between the longitudinal effective mass $m_\parallel$ and transversal effective mass $m_\perp$ ($K = m_\parallel / m_\perp$) and has been determined to be $K = 8.6$ for SnTe [25]. Using this K value, the semiaxis aspect ratio of the ellipsoidal pockets becomes $b = 2.9\,a$. For a magnetic field B applied parallel to the [111] direction, the cross-sectional area of the ellipsoidal Fermi surface belonging to the longitudinal valley is of circular shape ($S_F^L = \pi a^2$), as shown in Fig. 3(a). On the other hand, due to the inclination of 70.5° with respect to the longitudinal ellipsoid, the cross-sectional area of the oblique valleys will be an ellipse with semiminor axis equal to the radius a and semimajor axis equal to b' [$S_F^O = \pi a b'$, Fig. 3(b)].

Using the aspect ratio $b/a = 2.9$ and simple geometric relations, the ratio between the cross-sectional areas of the oblique and longitudinal pockets is calculated to be 2.1 ($S_F^O = 2.1 S_F^L$). Therefore, if we assume that the lowest frequency $f_1 = 137$ T is due to the bulk longitudinal valley and taking into account the Onsager relation [Eq. (2)], the frequency originating from the oblique valleys should also be 2.1 times larger than the frequency from the longitudinal

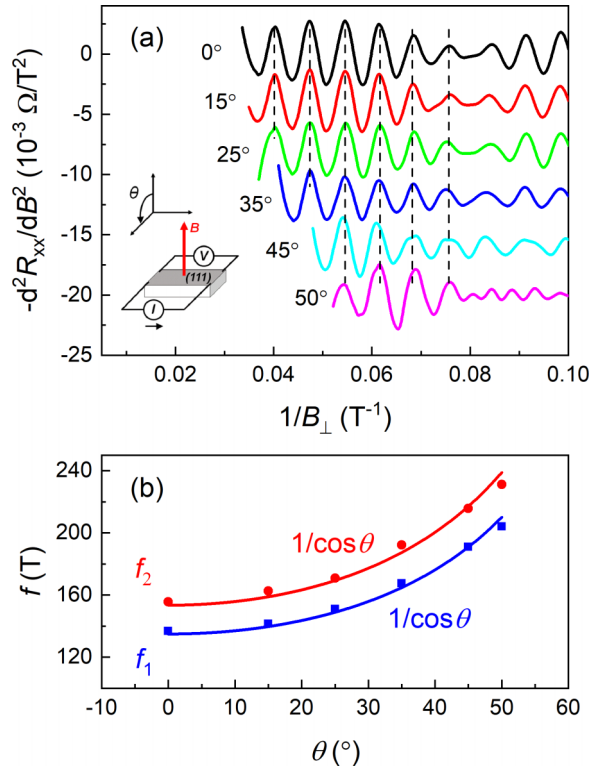

FIG. 4. (a) Angular dependence of the SdH oscillations in the longitudinal magnetoresistance R_{xx} measured at 4.2 K for increasing tilt angle θ from 0° to 50° (see inset for θ definition). The second derivative $-d^2R_{xx}/dB^2$ is plotted vs $1/B_\perp$ ($B_\perp = B\cos\theta$) and the curves are shifted for clarity. The extrema of the oscillations remain in the same position indicated by dashed lines. (b) Angular evolution of the two frequencies f_1 and f_2 obtained from the FFT analysis. The solid blue and red lines are the $1/\cos\theta$ fittings.

valley. Thus, since the measured ratio is $f_1/f_2 = 1.12$, we can assert that none of these frequencies originates from the oblique bulk Fermi pockets.

To further investigate the origin of the SdH frequencies, we studied the angular dependence of the longitudinal magnetoresistance for SnTe films. In Fig. 4(a) we plot the second derivative of $R_{xx}(B)$ as a function of $1/B_\perp$ ($B_\perp = B\cos\theta$) for several tilt angles θ from 0° to 50° [see inset in Fig. 4(a) for details on the measurement configuration]. For higher θ, the FFT frequencies cannot be clearly identified. As indicated by the dashed lines, it is evident that the same SdH pattern as a function of the perpendicular component of the field is reproduced for angles up to 50°. The two frequency components f_1 and f_2 obtained from the FFT analysis of the SdH oscillations are plotted in Fig. 4(b) as a function of the angle θ.

The angular evolution of both frequencies fits well with a $1/\cos\theta$ dependence, as demonstrated by the solid lines, indicating that the SdH oscillations only respond to the field component perpendicular to the surface. This $1/\cos\theta$ angle dependence is widely used as an indication of a two-dimensional (2D) charge transport and consequently attributed to the presence of surface states in literature, e.g., in TIs based on bismuth chalcogenides [14–20]. However, since SnTe possesses ellipsoidal bulk Fermi surfaces, the SdH oscillations from these bulk Fermi pockets can also present a $1/\cos\theta$

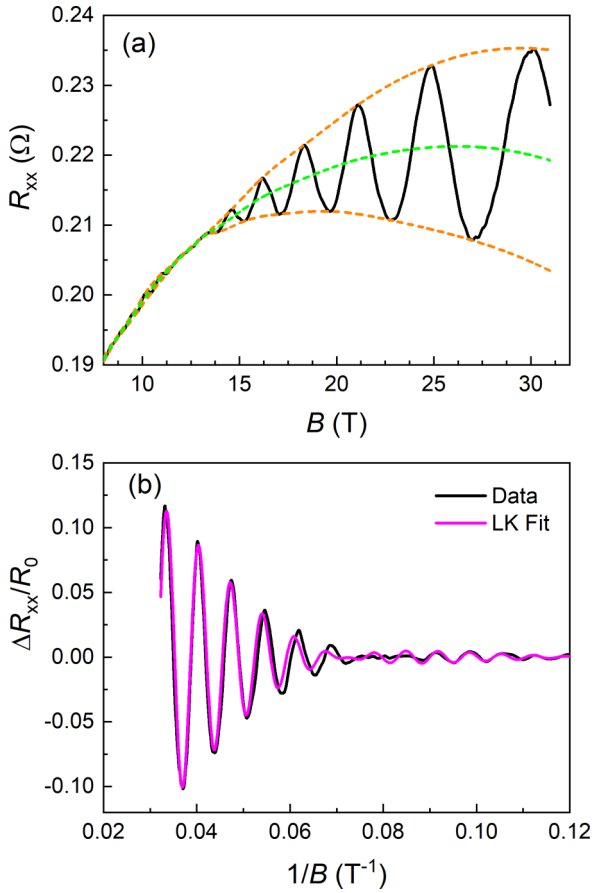

FIG. 5. (a) Envelope curves (orange dashed lines) obtained from the interpolation of the SdH oscillation extrema. The background (green dashed line) is the average between the upper and lower envelope curves. (b) Normalized oscillatory component $\Delta R_{xx}/R_0$ (black line) of the longitudinal magnetoresistance obtained after background subtraction of the raw data. The magenta line corresponds to the best fit using the complete Lifshitz-Kosevich expression given by Eq. (3). The two oscillatory components necessary to achieve the best fit are plotted separately in the graphs of Figs. 6(a) and 6(b).

dependence in this range of tilt angles. Hence, within this analysis we cannot conclusively distinguish whether the two SdH frequencies originate from a bulk or a surface channel.

In order to obtain more detailed information from the SdH oscillations we isolated the oscillatory component of the longitudinal resistance using the background subtraction method, as shown in Fig. 5. The envelope curves are obtained by interpolating the extrema (orange dashed line) of the oscillations. The background (green dashed line) is considered to be the average between these two envelope curves [Fig. 5(a)] Thus, the oscillatory component ΔR_{xx} is obtained after subtraction of the measured longitudinal resistance R_{xx} from the background curve. Figure 5(b) shows the normalized oscillatory component $\Delta R_{xx}/R_0$ (R_0 is R_{xx} at $B = 0$) as a function of $1/B$, where a beating pattern is clearly seen, in accordance with the second derivative result previously described [Fig. 1(b)].

The normalized oscillatory component $\Delta R_{xx}/R_0$ can be fitted with the complete Lifshitz-Kosevich expression [16]:

$$\frac{\Delta R_{xx}}{R_0} = \left(\frac{\hbar\omega_c}{2E_F}\right)^{\frac{1}{2}} \frac{\lambda}{\sinh(\lambda)} e^{-\lambda_D} \times \cos\left[2\pi\left(\frac{E_F}{\hbar\omega_c} + \frac{1}{2} + \beta - \delta\right)\right], \quad (3)$$

with the Fermi energy $E_F = \hbar^2 {k_F}^2/2m^*$, where k_F is the Fermi wave vector, $\lambda = 2\pi^2 k_B T/\hbar\omega_c$, and $\lambda_D = 2\pi^2 k_B T_D/\hbar\omega_c$, where the cyclotron frequency is given by $\omega_c = eB/m^*$ and T_D is the Dingle temperature. The phase offset β in the range from zero to one is associated with the Berry phase $\Phi_B = 2\pi\beta$. The value of $\beta = 0$ (or, equivalently, $\beta = 1$) corresponds to trivial fermions, whereas $\beta = 1/2$ is related to Dirac fermions with a π Berry phase [26–28]. The phase shift δ is the correction associated to the Fermi-surface dimension ($\delta = 0$ for the 2D Fermi surface and $\delta = -1/8$ or $+1/8$ for the 3D system with the extremal area of the Fermi surface given by a minimum or a maximum, respectively).

For the fitting process we used a fixed temperature ($T = 4.2$ K) and the values of the cyclotron mass m^* obtained above. To obtain a good fitting to the $\Delta R_{xx}/R_0$ data, it was necessary to consider the sum of two cosine terms with two different frequencies (k_{F1} and k_{F2}) and two phase offsets (β_1 and β_2). The parameters obtained after the best fit, shown by the magenta line in Fig. 5(b), are $k_{F1} = 0.0645$ Å^{-1} ($f_1 = 137$ T), $k_{F2} = 0.0684$ Å^{-1} ($f_2 = 154$ T), $\beta_1 - \delta = 0.03 \pm 0.01$, $\beta_2 - \delta = 0.21 \pm 0.01$, and $T_D = 46$ K. The two frequencies obtained by this LK fitting are identical to the values from the FFT analysis, confirming that result. The Dingle temperature T_D in the exponential decay term $e^{-\lambda_D}$ accounts for the oscillation damping with $1/B$. The mobility can be obtained from T_D by the relation $\mu = e\tau/m = e\hbar/2\pi m k_B T_D$, where τ is the carrier lifetime and the carrier effective mass $m = ({m_\perp}^2 m_\parallel)^{1/3} = 0.043\, m_e$, using $m_\perp = 0.021\, m_e$ and $m_\parallel = 0.18\, m_e$ [25]. A value of $\mu = 1080$ cm^2/V s is found for $T_D = 46$ K, in the same magnitude of the measured Hall mobility (1500 cm^2/V s).

The two oscillatory components needed to obtain the best fit within the LK expression are plotted separately in Figs. 6(a) and 6(b). The Landau-level (LL) fan diagram is obtained by assigning integers N to the oscillation minima and plotting the N indices as a function of $1/B$. Figure 6(c) exhibits the LL fan chart for the low-frequency (blue symbols) and high-frequency (red symbols) SdH oscillatory components together with the respective linear fit (blue and red lines). The phase factor $\beta - \delta$ can also be obtained by the intersection point with the N axis, determined by the linear extrapolation to $1/B = 0$, as highlighted in the inset of Fig. 6(c). Using this procedure, values of intercepts at -0.01 and 0.22 are found for the low- and high-frequency oscillatory components, respectively. As expected, these phase factors are very close to the values obtained by the LK fitting.

At this point, we conclude that normal fermions are involved in the magnetotransport of the low-frequency ($f_1 = 137$ T) oscillatory component, as its phase offset β_1 is very close to $0 \pm 1/8$, corresponding to a trivial Berry phase. This result associated with the analysis of the ratio between

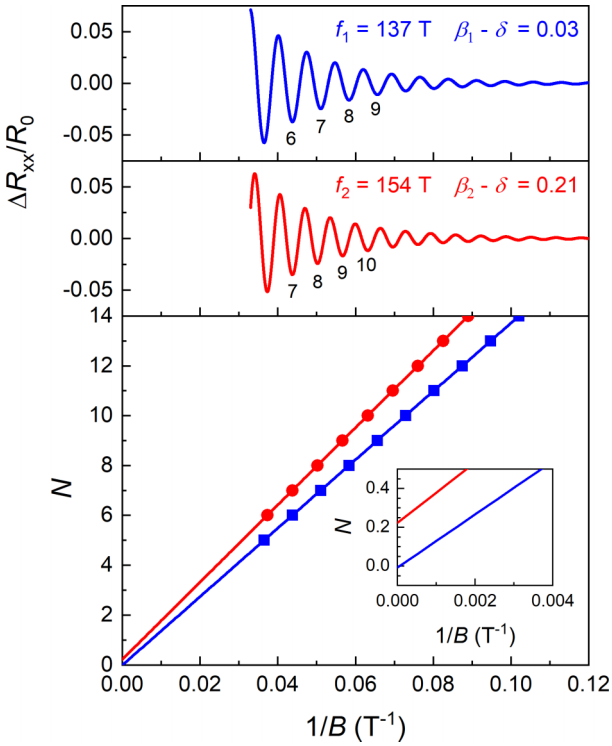

FIG. 6. (a) Low-frequency (137 T) and (b) high-frequency (154 T) oscillatory components needed to achieve the best LK fitting curve in Fig. 5(b). (c) Landau-level fan chart obtained by attributing integers N to the minima of the low-frequency (blue symbols) and high-frequency curves (red symbols) and plotting as a function of $1/B$. The blue and red lines are linear fits to the respective data. The linear extrapolation to $1/B = 0$ intercepts the N axis at -0.01 for the low-frequency and at 0.22 for the high-frequency oscillatory components, as highlighted in the inset. These intersections are very similar to the phase factors $\beta_1 - \delta = 0.03 \pm 0.01$ and $\beta_2 - \delta = 0.21 \pm 0.01$ obtained from the LK fitting.

the cross-sectional areas of the oblique and longitudinal SnTe Fermi surfaces demonstrates that this component is related to the bulk longitudinal valley.

On the other hand, the phase factor $\beta_2 - \delta = 0.21 \pm 0.01$ found for the high-frequency ($f_2 = 154\,\mathrm{T}$) oscillatory component suggests that it does not originate from a surface channel, as this value is different from the expected value $1/2 \pm 1/8$ for nontrivial Dirac fermions. In addition, the 3D-equivalent surface concentration calculated by p_{2D}/t, where $p_{2D} = {k_F}^2/4\pi$ and t is the film thickness, gives $1.6 \times 10^{16}\,\mathrm{cm}^{-3}$ for k_{F1} ($1.8 \times 10^{16}\,\mathrm{cm}^{-3}$ for k_{F2}). This value is three orders of magnitude lower than the hole concentration of a single bulk ellipsoid obtained by the relation $p_{3D} = {k_{Fa}}^2 k_{Fb}/3\pi^2$ ($k_{Fb}/k_{Fa} = 2.9$ for SnTe) that gives $p_{3D}(f_1) = 2.6 \times 10^{19}\,\mathrm{cm}^{-3}$ $p_{3D}(f_2) = 3.1 \times 10^{19}\,\mathrm{cm}^{-3}$]. This result suggests that the observed SdH oscillations do not arise from 2D states. Therefore, Berry phase and SdH carrier concentration analyses indicate that transport via surface channels is unlikely for SnTe films.

Another possible explanation for SdH oscillations formed by oscillatory components with closely spaced frequencies is the Rashba spin splitting. A beating pattern in the SdH

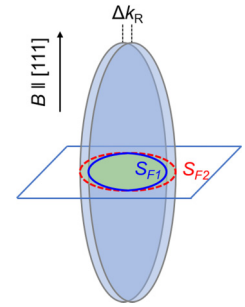

FIG. 7. Representation of the longitudinal ellipsoid with a Rashba spin-splitting Δk_R. For a magnetic field B applied parallel to the [111] direction, S_{F1} and S_{F2} represent the inner and outer extremal cross-sectional areas.

oscillations, analogous to the one found here for SnTe, is commonly observed in two-dimensional systems lacking inversion symmetry, such as gated InAs/GaSb quantum wells [29,30]. However, large Rashba splitting was detected also in bulk systems, such as BiTeI, leading to two sets of SdH oscillations, stemming from the inner and outer Fermi contours [31]. The Rashba splitting should additionally result in the nonzero Berry phase [30], as observed here for both oscillatory components. Furthermore, the spin-split S_{F1} and S_{F2} extremal cross-sectional areas (see Fig. 7) should also present a $1/\cos\theta$ angular dependence, in accordance with the behavior shown in Fig. 4(b). Moreover, considering that the SdH frequencies f_1 and f_2 are from the split bulk longitudinal ellipsoid and that the contribution of the oblique valleys (not observed here) should occur at a frequency $f_O = 2.1(f_1 + f_2)/2$, the total hole concentration $p_{SdH} = p_{3D}(f_1) + p_{3D}(f_2) + 3\,p_{3D}(f_O)$ (the factor 3 refers to three oblique valleys) gives $3.2 \times 10^{20}\,\mathrm{cm}^{-3}$, compatible with $p_{Hall} = 1.9 \times 10^{20}\,\mathrm{cm}^{-3}$ obtained by Hall measurements.

Figure 7 shows a schematic representation of the SnTe longitudinal ellipsoid with a Rashba splitting of Δk_R. This configuration leads to one inner and one outer Fermi contour that delineate the S_{F1} and S_{F2} cross-sectional areas. In this scheme, a Δk_R splitting value of $0.006\,\mathrm{Å}^{-1}$ is necessary to yield the frequency ratio $f_1/f_2 = S_{F1}/S_{F2} = 1.12$ observed in the SdH oscillations of SnTe films. Similar Rashba splitting ($\Delta k_R = 0.011\,\mathrm{Å}^{-1}$) has been found for Bi-doped $Pb_{0.54}Sn_{0.46}Te$ epitaxial films by ARPES measurements [13]. However, in that case symmetry breaking at the surface produces 2D Rashba bands, while our data clearly point towards a bulk mechanism. In the case of SnTe, the Rashba effect might arise from bulk traps, possibly originated from inhomogeneities or disorder in the lattice, that break the translation symmetry. A second possibility is related to the well-known low-temperature rhombohedral deformation of SnTe, which is expected to set in below 100 K for our range of carrier concentration [32,33]. Recent calculations indicate that the rhombohedral phase of SnTe is subjected to a large spin splitting for both the conduction and valence bands due to a Rashba mechanism [34]. Importantly, in Ref. [35] Plekhanov *et al.* have shown that this bulk splitting remains relevant also for partial (small) distortion of the cubic structure. In this scenario, the

Rashba splitting is related to the ferroelectric character of the material, which coexists with the TCI phase in SnTe.

IV. CONCLUSIONS

In summary, we measured the magnetotransport of (111) SnTe films grown on BaF_2 up to the high magnetic field regime (30 T). The longitudinal magnetoresistance R_{xx} exhibited clear and well-developed SdH oscillations at 4.2 K that remain up to 80 K. The second derivative $(-d^2R_{xx}/dB^2)$ versus $1/B$ curve showed a beating pattern and the FFT analysis of this curve revealed that the SdH oscillations are composed of two frequencies close to each other. The cyclotron mass corresponding to each frequency was determined by the FFT amplitude thermal damping.

A sequence of analyses was done in order to determine the origin of the SdH oscillations. The contribution of the oblique bulk Fermi ellipsoids to the oscillations is rejected by geometric arguments. In contrast to other TI materials, the $1/\cos\theta$ dependence observed for the two SdH oscillation frequencies is not sufficient to assure surface conduction, as the elongated SnTe bulk ellipsoidal Fermi surfaces also present the same angular dependence. The fitting of the oscillatory component of R_{xx} using the complete Lifshitz-Kosevich equation confirmed the two frequencies obtained in the FFT analysis and gave the Berry phase offset for each frequency.

The results of all these analyses indicate that the SdH oscillations of (111) SnTe thin films are constituted of two oscillatory components, compatible with Rashba splitting of the bulk longitudinal valley. The observation of split bulk valence bands in SnTe can be a pivotal indication for a novel phase with coexisting ferroelectric and TCI properties. Thereby, our results clearly call for further experimental effort on the SnTe material system.

ACKNOWLEDGMENTS

The authors acknowledge financial support from Brazilian Federal Agency for Support and Evaluation of Graduate Education (Grant No. 88881.131873/2016-01, international Ph.D. scholarship for A.K.O.) and Brazilian National Council for Scientific and Technological Development (Grants No. 302134/2014-0 and No. 307933/2013). We also acknowledge the support of the High Field Magnet Laboratory member of the European Magnetic Field Laboratory (Proposals No. NSC18-117 and No. NSC03-216).

[1] L. Fu, Phys. Rev. Lett. **106**, 106802 (2011).
[2] T. H. Hsieh, H. Lin, J. Liu, W. Duan, A. Bansil, and L. Fu, Nat. Commun. **3**, 982 (2012).
[3] T. Phuphachong, B. A. Assaf, V. V. Volobuev, G. Bauer, G. Springholz, L.-A. Vaulchier, and Y. Guldner, Crystals **7**, 29 (2017).
[4] V. A. Chitta, W. Desrat, D. K. Maude, B. A. Piot, N. F Oliveira, Jr., P. H. O. Rappl, A. Y. Ueta, and E. Abramof, Phys. Rev. B **72**, 195326 (2005).
[5] See Supplemental Material at http://link.aps.org/supplemental/10.1103/PhysRevB.98.195136 for additional information on the multivalley band structure of the $Pb_{1-x}Sn_xTe$ semiconductor compound and additional characterization of (111) SnTe epitaxial films: RHEED, AFM, x-ray-diffraction, temperature-dependent resistivity, and low-field Hall measurements.
[6] J. O. Dimmock, I. Melngailis, and A. J. Strauss, Phys. Rev. Lett. **16**, 1193 (1966).
[7] S. O. Ferreira, E. Abramof, P. Motisuke, P. H. O. Rappl, H. Closs, A. Y. Ueta, C. Boschetti, and I. N. Bandeira, J. Appl. Phys. **86**, 7198 (1999).
[8] E. Abramof, S. O. Ferreira, P. H. O. Rappl, H. Closs, and I. N. Bandeira, J. Appl. Phys. **82**, 2405 (1997).
[9] Y. Tanaka, Z. Ren, T. Sato, K. Nakayama, S. Souma, T. Takahashi, K. Segawa, and Y. Ando, Nat. Phys. **8**, 800 (2012).
[10] S.-Y. Xu, C. Liu, N. Alidoust, M. Neupane, D. Qian, I. Belopolski, J. D. Denlinger, Y. J. Wang, H. Lin, L. A. Wray, G. Landolt, B. Slomski, J. H. Dil, A. Marcinkova, E. Morosan, Q. Gibson, R. Sankar, F. C. Chou, R. J. Cava, A. Bansil, and M. Z. Hasan, Nat. Commun. **3**, 1192 (2012).
[11] Y. Tanaka, T. Shoman, K. Nakayama, S. Souma, T. Sato, T. Takahashi, M. Novak, K. Segawa, and Y. Ando, Phys. Rev. B **88**, 235126 (2013).
[12] C. Yan, J. Liu, Y. Zang, J. Wang, Z. Wang, P. Wang, Z.-D. Zhang, L. Wang, X. Ma, S. Ji, K. He, L. Fu, W. Duan, Q.-K. Xue, and X. Chen, Phys. Rev. Lett. **112**, 186801 (2014).
[13] V. V. Volobuev, P. S. Mandal, M. Galicka, O. Caha, J. Sánchez-Barriga, D. Sante, A. Varykhalov, A. Khiar, S. Picozzi, G. Bauer, P. Kacman, R. Buczko, O. Rader, and G. Springholz, Adv. Mater. **29**, 1604185 (2016).
[14] D.-X. Qu, Y. S. Hor, J. Xiong, R. J. Cava, and N. P. Ong, Science **329**, 821 (2010).
[15] Z. Ren, A. A. Taskin, S. Sasaki, K. Segawa, and Y. Ando, Phys. Rev. B **82**, 241306(R) (2010).
[16] J. Xiong, Y. Luo, Y. H. Khoo, S. Jia, R. J. Cava, and N. P. Ong, Phys. Rev. B **86**, 045314 (2012).
[17] J. G. Analytis, R. D. McDonald, S. C. Riggs, J.-H. Chu, G. S. Boebinger, and I. R. Fischer, Nat. Phys. **6**, 960 (2010)
[18] A. A. Taskin, S. Sasaki, K. Segawa, and Y. Ando, Phys. Rev. Lett. **109**, 066803 (2012).
[19] S. Wiedmann, A. Jost, B. Fauqué, J. van Dijk, M. J. Meijer, T. Khouri, S. Pezzini, S. Grauer, S. Schreyeck, C. Brüne, H. Buhmann, L. W. Molenkamp, and N. E. Hussey, Phys. Rev. B **94**, 081302(R) (2016).
[20] E. K. de Vries, S. Pezzini, M. J. Meijer, N. Koirala, M. Salehi, J. Moon, S. Oh, S. Wiedmann, and T. Banerjee, Phys. Rev. B **96**, 045433 (2017).
[21] A. A. Taskin, F. Yang, S. Sasaki, K. Segawa, and Y. Ando, Phys. Rev. B **89**, 121302(R) (2014).
[22] B. A. Assaf, F. Katmis, P. Wei, B. Satpati, Z. Zhang, S. P. Bennet, V. G. Harris, J. S. Moodera, and D. Heiman, Appl. Phys. Lett. **105**, 102108 (2014).
[23] R. Akiyama, K. Fujisawa, T. Yamaguchi, R. Ishikawa, and S. Kuroda, Nano Res. **9**, 490 (2016).
[24] K. Dybko, M. Szot, A. Szczerbakow, M. U. Gutowska, T. Zajarniuk, J. Z. Domagala, A. Szewczyk, T. Story, and W. Zawadzki, Phys. Rev. B **96**, 205129 (2017).
[25] X. Chen, D. Parker, and D. J. Singh, Sci. Rep. **3**, 3168 (2013).

[26] Y. Zhang, Y.-W. Tan, H. L. Stormer, and P. Kim, Nature (London) **438**, 201 (2005).

[27] K. S. Novoselov, A. K. Geim, S. V. Morozov, D. Jiang, M. I. Katsnelson, I. V. Grigorieva, S. V. Dubonos, and A. A. Firsov, Nature (London) **438**, 197 (2005).

[28] L. P. He, X. C. Hong, J. K. Dong, J. Pan, Z. Zhang, J. Zhang, and S. Y. Li, Phys. Rev. Lett. **113**, 246402 (2014).

[29] A. J. A. Beukman, F. K. de Vries, J. van Veen, R. Skolasinski, M. Wimmer, F. Qu, D. T. de Vries, B.-M. Nguyen, W. Yi, A. A. Kiselev, M. Sokolich, M. J. Manfra, F. Nichele, C. M. Marcus, and L. P. Kouwenhoven, Phys. Rev. B **96**, 241401(R) (2017).

[30] F. Nichele, M. Kjaergaard, H. J. Suominen, R. Skolasinski, M. Wimmer, B.-M. Nguyen, A. A. Kiselev, W. Yi, M. Sokolich, M. J. Manfra, F. Qu, A. J. A. Beukman, L. P. Kouwenhoven, and C. M. Marcus, Phys. Rev. Lett. **118**, 016801 (2017).

[31] H. Murakawa, M. S. Bahramy, M. Tokunaga, Y. Kohama, C. Bell, Y. Kaneko, N. Nagaosa, H. Y. Hwang, and Y. Tokura, Science **342**, 1490 (2013).

[32] M. Iizumi, Y. Hamaguchi, K. F. Komatsubara, and Y. Kato, J. Phys. Soc. of Japan **38**, 443 (1975).

[33] K. L. I. Kobayashi, Y. Kato, Y. Katayama, and K. F. Komatsubara, Phys. Rev. Lett. **37**, 772 (1976).

[34] X. Zhang, Q. Liu, J.-W. Luo, A. J. Freeman, and A. Zunger, Nat. Phys. **10**, 387 (2014).

[35] E. Plekhanov, P. Barone, D. Di Sante, and S. Picozzi, Phys. Rev. B **90**, 161108(R) (2014).